



# A novel hypothesis for the formation of conoidal projectile wounds in sandwich bones

John M. Rickman<sup>1</sup>  · James Shackel<sup>1</sup>

Received: 9 April 2018 / Accepted: 10 October 2018 / Published online: 18 October 2018  
© Springer-Verlag GmbH Germany, part of Springer Nature 2018

## Abstract

When perforated by a projectile, sandwich bones typically exhibit wounds with a distinct conoidal morphology that is widely utilised both in wound diagnosis and trajectory determinations. However, the dynamic fracture mechanisms underlying this intriguing wound type have yet to be experimentally verified. The most frequently quoted hypothesis for their formation, plug and spall, is difficult to reconcile with the conoidal morphology exhibited by such wounds. The present article carries out a high-speed videographic and micro-computerised tomographic ( $\mu$ -CT) analysis of perpendicularly produced projectile wounds induced from 139.15 to 896.84 metres per second (m/s) in pig scapulae. Fundamental data on energy absorption, wound shape and bevel symmetry are presented. Cross-sectional fracture morphology revealed by  $\mu$ -CT raises the novel hypothesis that tensile stresses induced by the projectile in the outer cortex elicit cone crack formation and that this cone crack then propagates catastrophically through the entire sandwich structure. This process results in the momentary formation of a bioceramic conoid, a conoidal volume of bone consisting of all three sandwich bone layers separated from the parent bone by the internal bevel. Fragmentation of the separated volume leaves the conoidal wound behind as its counterpart. The significance of this hypothesis in terms of differential diagnosis and interpretation of bevel shape is discussed.

**Keywords** Skeletal trauma · Projectile injuries · Forensic anthropology · Forensic pathology · Fracture · Sandwich bones

The potential of a bullet to incapacitate is determined by impact location and thus the anatomical structures damaged along the bullet tract [1], in addition to the amount of energy absorbed by those impacted tissues. In this regard, gunshot wounds to the cranial vault are exceptionally lethal. Mortality data summarised by Aarabi et al. [2] suggest that up to 71% of victims die at the scene of the shooting, whilst in the USA a 90% mortality rate has been reported in civilian settings [3]. From a forensic perspective, gunshot wounds to the sandwich bones of the skull are thus of considerable interest. In cross-section, sandwich bones are tri-layered structures consisting of two layers, or *laminae*, of cortical bone enclosing a lamina of trabecular bone [4]. Perpendicular entry

wounds to such bones typically consist of a circular fracture in the outer cortical layer and a larger cone-shaped area of damage involving the trabeculae and inner cortical layer termed the *bevel* [5], resulting in what may be described as a *conoidal wound*. Such conoidal wounds characteristically flare in the direction of projectile travel, resulting in an *internal bevel* in entry wounds and an *external bevel* in exit wounds [5]. Further trajectory determinations are based on areas of bevel elongation, which are thought to correspond to the specific direction of projectile passage [6, 7]. However, despite the clear importance of such determinations, the fracture mechanisms underlying formation of conoidal wounds remain unclear. In addition, the layers forming the bevel and other cross-sectional features of their microanatomy have to date received no formal definitions.

A significant step in establishing how conoidal wounds form in sandwich bones is identification of the bony layers through which critical fractures propagate to produce the final morphology. The cortical layer of the sandwich bone first impacted by the projectile is here defined as the *outer cortical layer* and its counterpart the *inner cortical layer*. The region where the trabecular bone meets a cortical layer is here defined

✉ John M. Rickman  
j.m.rickman@cranfield.ac.uk

James Shackel  
j.shackel@cranfield.ac.uk

<sup>1</sup> Cranfield Defence and Security, Cranfield University, Defence Academy of the United Kingdom, Shrivenham SN6 8LA, UK

as the *cortical-trabecular transition*, with one such region under the outer cortical layer and another above the inner cortical layer. In this paper, a crack propagating through a sandwich bone is defined as *inter-laminar* if it passes between layers and separates them (the process of *delamination*), *intra-laminar* if it occurs within a layer and *trans-laminar* if it crosses a layer (Fig. 1). Cracks are further classified as *mode 1* if produced by tensile stress (crack opening) and *mode 2* if produced by in plane shear, i.e. by one part sliding past another with no crack opening [8]. At present, the most widely accepted theory for conoidal wound formation is plug and spall [e.g. 9–11], which proposes that high tensile stresses initiated under the impacting projectile cause the shearing of a plug of bone from the outer cortical layer of the sandwich bone, which then moves ahead of the projectile through the other bone layers. According to this hypothesis, conoidal wound formation is a shear plugging process consisting of two phases:

1. Projectile entry through the outer cortical layer with associated shear plug formation
2. Bevel production during the process of projectile exit

Critically, this hypothesis proposes that bevel production occurs secondarily to plug formation; however, the specific biomechanical processes underlying bevel production by this cortical plug differ across the literature. Peterson [12] suggested that the cortical disc of bone is pushed through the trabecular layer and then blows out the bevel on the inner layer. Komar and Buikstra [9], Symes et al. [10] and Christensen et al. [11] suggested that spall, or fracture, produces the internal bevel without speculating on the stresses involved, whilst Kimmerle and Baraybar [13] suggested that bevelling is created by the plug shearing through the trabeculae. Kieser et al. [14] used micro-computerised tomography to analyse cross-sections of pig ribs perforated by 0.22 handgun projectiles and reported a clear transition between a vertically walled channel through the outer cortical layer and the conoidal bevel beneath. Utilising this interpretation of the wound cross-section, these authors suggested that the sheared cortical plug, together with accumulated fractured material ahead of it, causes internal bevel production through a process of brittle fracture. These theories notwithstanding, it remains unclear as to why, specifically, a conoidal morphology is formed by the plug and spall mechanism, and nor is it clear how a cortical plug could withstand the massive stresses of the impact event without itself fragmenting during the perforation process.

An implicit assumption of the plug and spall hypothesis is that trans-laminar fracture is limited to the outer cortical layer, resulting in production of a plug consisting solely of cortical bone. However, recent descriptions of conoidal wounds associated with intact tri-layered bone plugs in both archaeological and recent material raise the intriguing hypothesis that all three

layers of the sandwich bone might fracture as a unit during projectile impact due to trans-laminar fracture propagation through the entire structure. The first description of such plugs was provided by Murphy et al. [15] who described frontal and parietal plugs associated with perforating wounds of unknown aetiology in archaeological material. Murphy et al. [16] later described two more entry wound plugs in a parietal (produced by impact with a train) and occipital (produced by a cross-bow bolt), and Bird and Fleischman [17] later provided additional information on a frontal bone exit wound plug produced by low-velocity bullet impact. Significantly, these tri-layered bone plugs are conoidal and the hole they fit into in their parent bone is bevelled accordingly, internally for an entry [15, 16] and externally for an exit [17]. The compressive side of the plug in the outer cortical layer may exhibit compressive damage, whilst the tensile side of the plug in the inner cortical layer is often characterised by radial fractures emanating from a central point, a process resulting in a distinct *stellate fracture* pattern. Although this limited number of reports testifies to tri-layered plug formation during at least some low energy impacts, it is currently unknown if their production is fundamental to conoidal wound formation or if these rare examples are atypical in nature.

A number of questions may be posed in relation to the mechanisms underlying conoidal wound formation. Firstly, what plugging mechanisms are operative during projectile perforation of sandwich bones; i.e. is trans-laminar fracture isolated to the outer cortical plate or does it involve all three layers? Secondly, is the same plugging mechanism operative at different velocities? Thirdly, if a role for tri-layered plugs is suggested by conoidal wound morphology, by what mechanisms are they formed? Fourthly, how might these mechanisms influence wound morphology? Fifthly, does projectile impact initiate internal damage peripheral to the conoidal wound? In order to begin to address these questions, the present paper presents the findings of a high-speed video and micro-computerised tomographic ( $\mu$ -CT) analysis of a series of experimentally induced projectile wounds inflicted at a series of increasing velocities to porcine scapulae. Gross wound morphology is described and basic data on energy absorption by sandwich bones during perforation is established. Based on this investigation, a nomenclature for the cross-sectional microanatomy of projectile wounds is developed and a novel theory for the formation of conoidal wounds is presented.

## Methods

### Projectile type and characteristics

Projectile yaw (deviation from horizontal flight) and deformation significantly affect the amount of energy absorbed during tissue penetration. In order to eliminate the effects of these

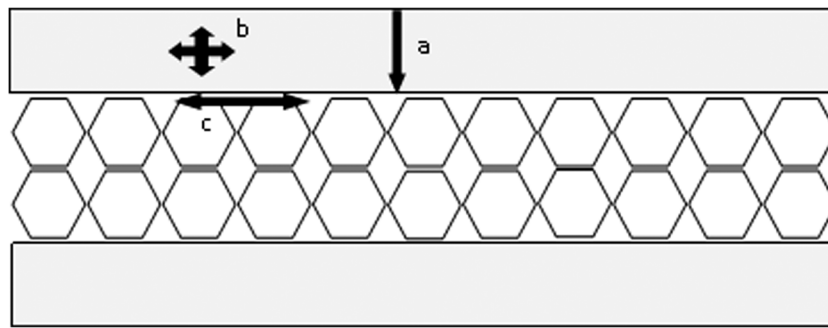


**Fig. 1** Fracture classification scheme utilised for cracks in sandwich bones; outer cortical layer (top rectangle), inner cortical layer (bottom rectangle) and trabecular layer represented by hexagons. (a) *Trans-*

*laminar fracture* crosses a lamina. (b) *Intra-laminar fracture* occurs within a lamina and may occur in any direction. (c) *Inter-laminar fracture or delamination* occurs between laminae

variables on fracture processes, surface hardened carbon steel spheres (Atlas Ball and Bearings Co. Ltd., UK) were utilised. Sphere weight and calibre were calculated from 24 spheres. Projectile calibre was measured using digital sliding callipers measuring to one hundredth of a millimetre. To determine projectile hardness, four spheres were ground and polished, mounted in polyester resin and then tested in a HWDM Indentec Micro indenter (Indentec Ltd., UK); ten readings were taken for the surface hardened exterior and ten for the core of each projectile. Mean hardness for each region was calculated from all four projectiles. Mean Vickers hardness values and projectile specifications are presented in Table 1. High Vicker's hardness and observation of high-speed footage indicated that projectile deformation could be eliminated from consideration in wounding processes.

### Sample selection

Given both the rarity and ethical implications of utilising human bone, this material was considered unsuitable for preliminary investigation. The scapulae of large domesticated artiodactyls, including the cow (*Bos taurus*) and pig (*Sus scrofa*), are sandwich bones that exhibit internally bevelled wounds when subjected to ballistic impact. As such, their suitability as surrogates for the human cranium in experimental ballistic work has been discussed previously [18, 19]. Pig scapulae are smaller and therefore easier to machine, store and secure during testing than cow scapulae and were therefore selected for this experiment.

### Sample preparation and velocity groups

Frozen pig scapulae were obtained from animals killed humanely as part of the food chain; samples were only taken from animals 12–14 months of age to ensure ossification of the target region. Specimens were stored frozen in sealed plastic bags at all times apart from when being prepared and impacted. The infraspinous fossa was selected as the impact region due to its larger size; only specimens with soft

tissue in this region were utilised. Selected shot direction was lateral to medial, allowing the bevel to form in the flatter subscapular plate. In order to create specimens with a relatively uniform plate configuration, frozen specimens were machined on a bandsaw to approximately 120 mm height; as much of the scapular spine as possible was also removed (Fig. 2).

Target location in the scapulae was chosen to be 40–50 mm from the nearest edge; once selected, the location was marked with an ink dot. In order to examine wounds inflicted across a series of velocities and to allow comparison of impact data, fleshed specimens were allocated into one of five velocity groups. Each velocity group was allocated a target impact velocity;  $V_1$  (150 m/s),  $V_2$  (350 m/s),  $V_3$  (450 m/s),  $V_4$  (650 m/s) and  $V_5$  (850 m/s), with groups  $V_2$  and  $V_5$  encompassing muzzle velocities of common handgun and rifle ammunition, respectively. To capture examples of soft and hard tissue behaviour during projectile exit, the camera was moved to face the rear of selected specimens. Using this mechanism, exit was filmed in one fleshed  $V_1$  specimen and one fleshed  $V_2$  specimen. To fully visualise bone fracture behaviour during exit, five additional specimens were defrosted and soft tissue dissected away from the inner cortical plate (group D); these specimens were impacted between 139–146 m/s. All specimens were defrosted slowly at room temperature in their sealed bags before the ballistic tests.

**Table 1** Projectile characteristics, standard deviations in parentheses

Material	Mean surface hardness (Vickers) ( $n = 10$ )	Mean core hardness (Vickers) ( $n = 10$ )	Mean diameter (mm) ( $n = 24$ )	Mean weight (g) ( $n = 24$ )
Surface hardened carbon steel	717 (33.75)	455 (28.13)	5.98	0.885

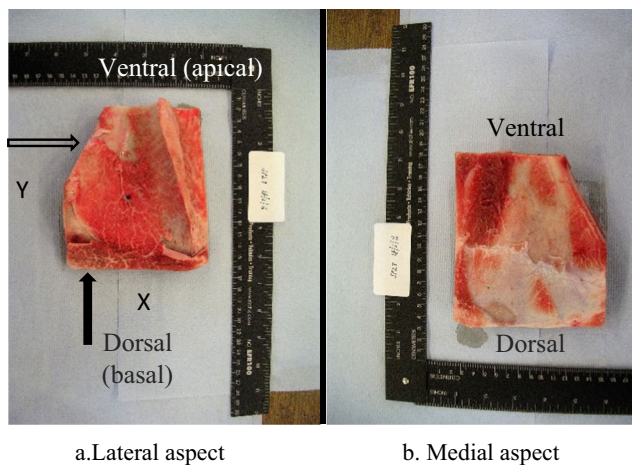


**Fig. 2** Machined plate of sandwich bone with soft tissue covering orientated in shooting position. Anatomically ventral portion of scapula formed the apex of the plate during shooting. Letters x and y in **a** denote the axes utilised in  $\mu$ -CT analysis; z-axis (not shown) refers to the depth of the specimen. Longitudinal (y-z) section indicated by open arrow; transverse (x-z) section indicated by closed arrow; x-y section descends through the depth of the plate. **a** Lateral aspect. **b** Medial aspect

### Shooting equipment and high-speed filming

The response of bone to loading is strongly influenced by the direction in which it is loaded; that is, bone is anisotropic [20]. In order to reduce the influence of loading direction on wounding patterns, all specimens were mounted with the broad, anatomically dorsal region acting as the base and the narrower ventral region acting as the apex. Specimens in groups  $V_1$ – $V_3$  were impacted using a compressed air powered 21.3-mm calibre gas gun with a 12-cm muzzle-target distance; projectiles were held in a plastic holder (sabot) during firing which fragmented on a metal sabot stripper after exiting the barrel. To approach the desired velocities in the last two velocity groups, an initial round of 12 impacts across groups  $V_4$  and  $V_5$  utilised a 30-mm helium powered gas gun; however, in all but two impacts high-velocity plastic sabot fragments were found to have damaged the impact area. Accordingly, a further 13 specimens in groups  $V_{4-5}$  were prepared and impacted using an Enfield number three proof housing with a 7.62-mm barrel; projectiles were sabot mounted and fired from a cartridge using a muzzle-target distance of 3.80 m to prevent sabots from impacting the specimens. Projectile perforation in defleshed  $V_6$  specimens was achieved using a compressed air-powered gas gun, capable of velocities approaching 150 m/s.

Phantom high-speed cameras were utilised to obtain high-speed footage of all impacts (Vision research, New Jersey). A Phantom v12 camera operating at 55009 frames per second was utilised for both side and exit footage in the gas gun experiment. Specimen location during exit filming in the gas gun chamber prevented lateral placement of a second camera for velocity determination; accordingly, velocity was determined using the gas gun's time gate. High-speed footage for

$V_4$  and  $V_5$  was obtained using a Phantom v1212 camera at 37000 frames per second.  $V_6$  exit footage was obtained using a Phantom v1212 camera at 40,000 frames/s, whilst lateral footage was obtained using a Phantom v7 camera operating at 5500 frames/s. Differences in cameras utilised were based solely on equipment availability and the maximum frame rate possible was utilised for each experimental set up. A millimetre scale was placed in view of the camera during filming to allow subsequent velocity determinations. To calculate incident (pre-impact) and residual (post-impact) projectile velocities, the camera was placed to the side of the impacted specimens. Velocities were then determined using Phantom Cine Viewer on a laptop. To allow for variation in the estimation of velocity caused by blurring of the projectile edges, the frame offering the best view of the projectile was selected and a clear location on the projectile noted. Velocity determinations were made using the same frame and location on the projectile on three separate occasions; projectile velocity was taken to be the mean of these three determinations.

### Kinetic energy and energy absorption calculations

The kinetic energy,  $E$ , in joules, of a projectile of mass  $m$  (in kilogrammes) and velocity  $v$  (in metres per second, m/s) is given by:

$$\frac{mv^2}{2} \quad (1)$$

During penetration, the kinetic energy of the projectile is transferred to the tissues and utilised to do mechanical work, manifested as tissue wounding. If the projectile retains kinetic energy and exits the impacted body, and if there is no change in mass of the projectile, the kinetic energy absorbed ( $\Delta E$ ) is equal to the difference between the incident kinetic energy ( $E_i$ ) and residual kinetic energy ( $E_r$ ) and is given by:

$$\frac{m(v_1^2 - v_2^2)}{2} \quad (2)$$

where  $V_1$  is the incident velocity and  $V_2$  the residual velocity.  $E_i$ ,  $E_r$  and  $\Delta E$  were calculated for each perforation event and the mean of these values determined for each velocity group. The amount of energy utilised to perforate the bone in relation to available incident kinetic energy was expressed as a percentage using the formula  $\Delta E/E_i \times 100$ . In order to determine the error associated with  $\Delta E$  values for each individual perforation event, which was calculated from the mean of three velocity determinations, an error propagation formula was generated. The error propagation formula propagates the standard deviations of the projectile velocity and mass measurements in order to provide a standard deviation for the energy absorbed,  $[\sigma_{\Delta E}]^2$ :

$$[\sigma_{\Delta E}]^2 = \left[ \frac{v_1^2 - v_2^2}{2} \right]^2 [\sigma_m]^2 + \left[ \frac{v_1}{2} \right]^2 [\sigma_{v_1}]^2 + \left[ \frac{v_2}{2} \right]^2 [\sigma_{v_2}]^2 \quad (3)$$

where  $\sigma$  is the standard deviation and  $m$  is the mass of the projectile in kilogrammes,  $v_1$  is the impact velocity and  $v_2$  the residual projectile velocity. The standard deviation associated with the kinetic energy absorbed for each individual impact is calculated by taking the square root of  $[\sigma_{\Delta E}]^2$ .

### Impacted specimen analysis and micro-computerised tomography

In order to retain structural features critical to morphological analysis such as displaced bone fragments, soft tissue was left in situ for scanning. Long scan times and large sample size necessitated re-freezing impacted bones to prevent soft tissue decomposition prior to scanning. After impact, the bones were placed into a sealable bag, wrapped in protective tissue and frozen.

For  $\mu$ -CT analysis, specimens were scanned in an X-Tec XT H 225  $\mu$ -CT (Nikon, Japan). In order to maximise resolution, the wound region was selected and observed at 75 kV, 90  $\mu$ A and 2.25 magnification, giving a voxel size of 89  $\mu$ m. The scanned volumes were manually reconstructed using Nikon's CT Pro 3D software; to eliminate edge artefacts, the radius of reconstruction was reduced from 100 to 90–95% depending on specimen size and the location of the wound. Volumes were analysed in VGStudeo MAX version 2.2 (Volume graphics, Germany). In order to allow comparison of x-z (transverse) and x-y (longitudinal) planes in VGStudeo MAX, a simple registration was carried out; each sectional plane was orientated so that the specimen occupied the centre of the screen with the cortical entry wound uppermost. In order to use the software's measuring tools, the bone surfaces were identified and highlighted using the surface determination function, which allows the user to specify the background and the material of interest.

### Controls

To determine if re-freezing impacted bones resulted in damage alteration, a shot control was  $\mu$ -CT scanned pre- and post-freezing to allow comparison of damage areas. Surface determination and simple registration were performed on pre- and post-freeze scans. Three damaged and displaced cortical bone regions in the pre-freeze scan were selected and the software's measuring tool utilised to measure the straight line distance in millimetres between two readily identifiable points in each of these damaged areas. To aid identification of the same landmarks in the post-freeze scan, an image of each location in the pre-freeze scan was saved as a JPEG file. The post-freeze scan

was then opened and landmarks identified using the appropriate JPEG image; straight line distances between the same points were then measured and compared to pre-freeze measurements.

### Gross wound morphology

Cortical entry wounds were classified as circular, oval, irregular or a combination of these; circular-irregular or oval-irregular wounds were classified as wounds with irregularity occurring in part of the otherwise symmetrical wound margin. Based on cross-sectional views obtained using  $\mu$ -CT, the internal bevel was defined as a fracture surface encompassing the trabeculae and the fracture edge of the inner cortical layer. Following Quatrehomme and İscan [21], internal bevels were defined as symmetrical if the bevel formed an evenly distributed wound margin and asymmetrical if any part of the perimeter was noticeably more pronounced. Preliminary  $\mu$ -CT analysis indicated that the internal bevel is present beneath retained inner cortical plate fragments and these were thus considered part of the bevelled area when determining bevel symmetry. The relationship between the shape of the cortical entry wound and the shape of the internal bevel was assessed utilising  $\mu$ -CT in both sectional and three-dimensional views.

### Results

A total of 47 specimens were perforated; 13 specimens from groups  $V_{4-5}$  were excluded from analysis due to plastic sabot damage in the 30-mm gas gun chamber or off target impacts when using the projectile housing apparatus. Of the remaining 34 sandwich bones, only the fully fleshed specimens ( $n = 29$ ) were scanned in the  $\mu$ -CT and utilised for subsequent computerised analysis. A total of seven inner plate cortical exits were filmed, five with soft tissue removed and two with soft tissue in situ.

### Controls

Comparison of pre- and post-freeze wounds suggested that freezing did not alter gross wound structure. Differences in measurements between pre-freeze and post-freeze scans were 30  $\mu$ m, 10  $\mu$ m and 10  $\mu$ m, respectively. Such sub-millimetre differences between pre- and post-freeze measurements are likely attributable to small variation in surface determinations between scans, to fine differences in placement of each end of the measurement tool and to the possibility that the selected post-freeze measurement location did not fully correspond exactly to the pre-freeze measurement location.

## Kinetic energy absorption and gross wound morphology

The total range of impact velocities was 139.15 m/s to 896.84 m/s; all specimens were fully perforated. Mean incident kinetic energies and mean absorbed kinetic energies are provided for each velocity group in Table 2. Mean absorbed kinetic energy in group  $V_5$  was 10.73 times greater than in group  $V_1$ . An increase in incident kinetic energy resulted in an increase in the amount of energy absorbed. The percentage of available incident kinetic energy absorbed during perforation was inversely related to velocity; whilst just under half of incident kinetic energy was absorbed during perforation in  $V_1$ , less than a quarter was absorbed in  $V_5$ .

Observation of soft tissue post-impact revealed a dusting of sabot fragments in the soft tissue around the perforation site. Whilst some wound irregularity due to sabot impact cannot be fully ruled out, their presence around both circular and irregular wounds suggested any such effects were absent or minimal. Table 3 provides sample data on gross wound morphology across the five velocity groups. Only group  $V_1$  exhibited the same entry wound shape in all perforated specimens, with all being circular. Increased incident velocity resulted in greater variation in cortical entry wound shape between specimens and an increase in occurrence of irregular wounds. Despite this general trend, there was overlap in entry wound morphology across groups  $V_2$ – $V_5$ . In total, the majority of wounds (48.26%) were circular, followed by irregular (27.59%), circular-irregular (13.79%), oval-irregular (6.90%) and oval (3.45%). The majority of wounds exhibited asymmetrical bevelling (82.76%), whilst symmetrical bevelling was present in only 17.24% of wounds. The high frequency of bevel asymmetry meant that, of the 14 circular entry wounds, only two (in group  $V_1$ ) exhibited a symmetrical bevel. Excluding four specimens across  $V_4$  and  $V_5$  where extensive cortical plate damage prevented accurate analysis, irregular cortical entry shape was lost by the internal bevel in 8/10 of the remaining irregular or partially irregular wounds.

There was variation in the extent of damage within groups at higher velocity; for example, whilst one specimen in  $V_4$  and three specimens in  $V_5$  exhibited considerable internal and external cortical plate damage at the impact location, other specimens in these groups showed far less damage despite similar energy absorption values. For example, in  $V_5$  one specimen was perforated at 851.92 m/s, absorbed 60.39 J of energy and exhibited extensive damage to both external and internal plates; another, impacted at 871.02 m/s and absorbing 56.32 J, presented with a neat circular entry with a slightly depressed top margin.

**Table 2** Mean incident kinetic energy ( $E_i$ ), mean residual kinetic energy ( $E_r$ ), mean absorbed kinetic energy ( $\Delta E$ ) and mean percentage kinetic energy absorbed

Velocity group	$E_i$ (J)	$E_r$ (J)	$\Delta E$ (J)	Percentage	Range $\Delta E$ (J)
D ( $n = 5$ ) <sup>a</sup>	8.93 (0.27)	3.72 (1.06)	5.21 (1.07)	58.37 (12.11)	3.32–6.40
$V_1$ ( $n = 6$ ) <sup>b</sup>	11.58 (0.95)	5.80 (0.88)	5.78 (0.72)	49.98 (5.32)	5.18–7.13
$V_2$ ( $n = 4$ ) <sup>b</sup>	55.45 (4.77)	40.27 (6.06)	15.18 (1.31)	27.68 (4.68)	13.46–16.63
$V_3$ ( $n = 3$ )	93.20 (1.17)	70.33 (3.43)	22.87 (4.58)	24.48 (4.57)	18.72–29.24
$V_4$ ( $n = 5$ )	191.06 (31.93)	148.37 (21.12)	42.69 (13.78)	22.04 (4.02)	32.18–63.65
$V_5$ ( $n = 7$ )	318.24 (37.38)	256.19 (29.80)	62.05 (13.14)	19.43 (2.86)	42.38–86.72

All energy data in joules with standard deviations in parentheses

<sup>a</sup> Group D specimens had soft tissue dissected from the inner cortical plate prior to perforation, resulting in an unquantified reduction in energy absorption

<sup>b</sup> Two specimens from  $n = 8$  in  $V_1$  and two of  $n = 6$  specimens in  $V_2$  were utilised for perforation filming in a confined gas gun chamber that would not fit two high-speed cameras; velocities could thus not be determined from lateral high-speed footage

## High-speed footage of inner plate perforation and $\mu$ -CT imaging of exit damage

Observation of the inner cortical plate during projectile exit at  $\times 4$  magnification failed to detect the ejection of a disc of bone corresponding to a sheared plug from the outer cortical layer, although fragmentation of such a structure once formed cannot be ruled out. High-speed footage revealed that tensile stellate fracture of the inner cortical plate was a significant component of the exit process. This fracture type, consisting of numerous radial cracks emanating from a central region of the exit, was clearly observed in three out of the five defleshed specimens and in both fleshed specimens; projectile exit was out of frame in two defleshed perforation events but an apparent stellate fracture was visible in a detached circular fragment in one of these (see below). Figure 3 shows a typical example of projectile exit in a defleshed inner plate at 142.51 m/s, with Fig. 3a showing the plate just before exit is initiated (designated time 0). The first indication of the perforation event was a small circular elevation of the cortex in the region that will form the location of the bevelled exit (Fig. 3b); although small, this elevation was detectable when compared to the non-perforated inner plate (Fig. 3a). Within 25  $\mu$ s, the elevation had increased in height and exhibited three radial fractures emanating from its apex (Fig. 3c), forming a distinct stellate fracture that demarcated at least three triangular bone fragments (highlighted in Fig. 3d). As projectile exit proceeded, the cortical fragments elevated (Fig. 3e) and then

**Table 3** Entry wound shape and bevel symmetry for  $n = 29$  sandwich bone perforation events. Morphology determined in fleshed specimens using  $\mu$ -CT in order to preserve fragile fractured elements on the inner cortical plate

Velocity group	Circular	Oval	Irregular	Circular-irregular	Oval-irregular	Bevel symmetry	
						S	A
$V_1$	8					2	6
$V_2$	1		2	2	1	2	4
$V_3$			2	1		0	3
$V_4$	3	1	1			0	5
$V_5$	2		3	1	1	1	6
Total	14	1	8	4	2	5	24
Percentage	48.26	3.45	27.59	13.79	6.90	17.24	82.76

S symmetrical, A asymmetrical

everted, resulting in their internal faces being uppermost (Fig. 3f). Cortical fragments were then either detached from the inner plate to form larger components of the ejecta plume or remained in situ. Measured from time zero to when the projectile was fully visible, the exit process took a total of 0.225 s at 142.51 m/s.

The crack forming the perimeter of the region of stellate fracture, here designated the *exit cortical fracture edge*, formed the cortical margin of the internal bevel. The radial tensile cracks composing the stellate fracture always arrested at this edge, a phenomenon also clearly visible in  $\mu$ -CT images of perforated inner cortical plates (see Fig. 4). This crack arrest process indicates that the internal bevel must form very early during perforation and before radial crack production and dictates that bevel shape and symmetry is largely determined before the projectile has exited the bone. In one 142.52 m/s perforation, an approximately circular structure consisting of a fractured inner plate of cortical bone was captured moving ahead of the projectile (Fig. 4a). This removed circular section corresponded in part-counterpart fashion to the bevelled exit beneath it, and it thus represented the cortical floor of the conoidal wound volume (Fig. 4a, thick arrow). The central portion of this circular plate presented a faint rhomboidal pattern with a centrally located apex, indicating stellate fracture had initiated but not completed there (Fig. 4a, thin arrow). In this specimen, fracture of the inner cortical plate during bevel formation allowed displacement of a complete disc of cortical bone. Due to the angle of observation, it was not clear if this circular structure was composed of all three sandwich bone layers. Observation of exit in fleshed specimens at both low (168 m/s) and moderate (333 m/s) velocity revealed the same sequence as observed in defleshed specimens. A small elevation appeared, which then grew in height; the walls of this elevation, although covered in soft tissue, were clearly triangular in shape and formed by stellate fracture (Fig. 4b). The fragments then proceeded through the processes of elevation and eversion before being ejected.

A series of  $\mu$ -CT images of inner cortical plate damage morphology is provided in Fig. 4c–f. Triangular fragments on the inner plate of specimens in  $V_1$  and  $V_2$  were often left in an elevated position forming *fragment cones* (Fig. 4c–d), and when present the region of convergence of the elevated fragments represented the point of projectile exit (Fig. 4d–e). Subsequent to higher velocity impacts in groups  $V_2$ – $V_5$ , inner plate fragments remained confined within the margin of the exit cortical fracture edge but often presented with semi-lunar or rectangular form (Fig. 4f, thin arrow), with a fractured distal border indicating loss of material in the ejecta plume (Fig. 4f).

### $\mu$ -CT fracture analysis of projectile wounds

$\mu$ -CT analysis revealed a number of internal morphological features of perforating wounds to sandwich bones and the following nomenclature was developed for analysis. An annotated cross-section typical of perforations across the series is shown in the  $y$ - $z$  (longitudinal) plane in Fig. 5. In cross-section, the conoidal morphology of such perforating wounds is readily apparent. The *cortical entry wound* (1) is delineated by an *entry cortical fracture edge* (2). The fractured edges of the trabeculae are discernible and form a *trabecular fracture margin* (3). The *peripheral trabeculae* (4) may be classified as trabeculae up to 3 mm peripheral to the trabecular fracture margin. The *cortical exit wound* (5) is delineated by an *exit cortical fracture edge* (6). In current terminology, the *trabecular fracture margin* and *exit cortical fracture edge* would together constitute the *internal bevel* (7); however, in-line fracture between the entry cortical fracture edge and the trabecular fracture margin immediately beneath it makes the definition of what layers constitute the internal bevel somewhat arbitrary. The *cortical entry wound* and *internal bevel* together constitute the *wound volume* (8). Although *trabecular intrusion* into the wound volume was observed in some sections (see Fig. 6b), a distinct feature of the wound volume in

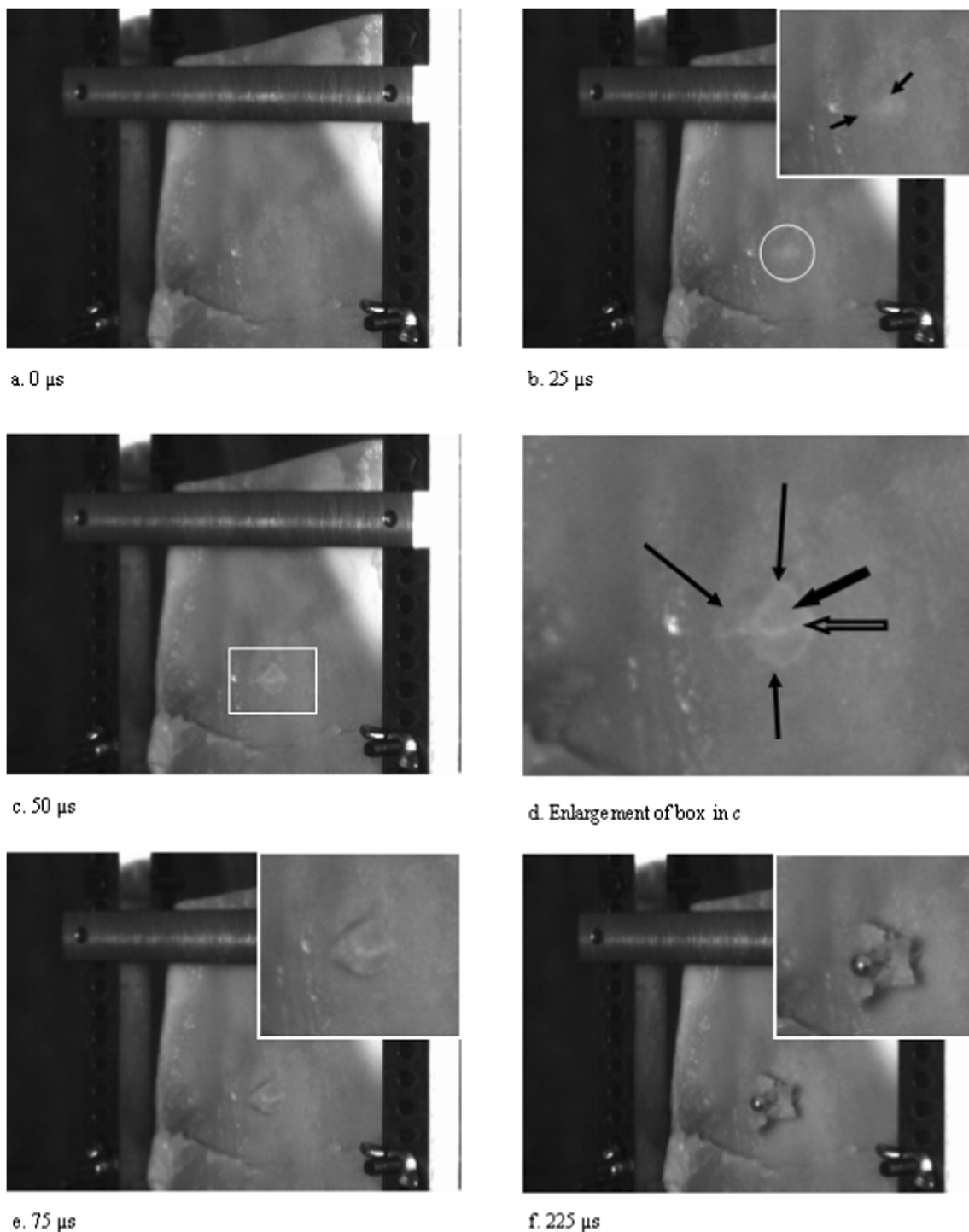


**Fig. 3** Projectile exit, soft tissue removed, incident velocity 142.51 m/s ( $\sigma$  0.61); **a** Pre-impact. **b** Initial cortical elevation visible as whiter region; enlargement inset shows faint indications of stellate fracture (arrows). **c** Fracture cone (highlighted). **d** Enlargement of fracture cone. Note

example of radial fracture (large open arrow) and inner cortical plate fragment (large closed arrow). Thin arrows denote margin of external bevel, the *exit cortical fracture edge*; note that radial fractures arrest at this feature. **e** Plate elevation. **f** Plate eversion

the trabecular region is an abrupt border formed by the free edges of fractured trabecular cells.

In section, a characteristic feature of the entry cortical fracture edges is their angulation with respect to the cortical surface, a structure conforming to the typical cone crack

morphology observed in impacted non-biogenic brittle materials such as ceramics (Fig. 6a–c). This cone crack type morphology was observed in 25 specimens across the five velocity groups; only four specimens with extensive damage to both cortical layers did not exhibit bilateral angulation at some



point in the cross-section. Mean cortical angles of the entry cortical fracture edge were obtained using the angle measuring tool in VGStudeo MAX; the y-z plane (longitudinal) was utilised to avoid any effects induced by curvature of the scapular fossae in the transverse direction. Results for the apical and basal sides of the wounds are presented in Table 4. Mean cortical angles differed on each side of the wound, with mean basal angles showing less variation than mean apical angles. Individual cortical angles showed considerable overlap across the velocity groups with no apparent association with velocity.

Analysis of fracture propagation at the upper cortical-trabecular interface revealed that, rather than adopting an inter-laminar course, the crack initiated in the outer cortex entered the trabeculae and extended through to the exit cortical fracture edge on the same side, producing a continuous trans-laminar fracture margin through the wound channel and resulting in an internal conoidal symmetry (Fig. 6a–c, e). This conoidal symmetry and common fracture edge through the three layers was found in all velocity groups and was thus independent of the absorbed kinetic energy. Lack of inter-laminar fracture at the cortical-trabecular interfaces meant that no specimens showed any evidence of delamination of the sandwich structure around the circumference of the wound channel. Pronounced intra-laminar fracture between cortical layers, produced by lateral deviation of the crack tip *within* the trabecular region, was observed in two thin specimens in groups  $V_1$  and  $V_5$  and one thicker specimen in  $V_1$ . The latter specimen, perforated at 166.56 m/s, deviated markedly from the typical wounding pattern (Fig. 6d). In longitudinal (y-z) section, this wound presented with a cylindrical wound channel to approximate mid-trabecular depth; at this point, the trabecular fracture margins deviated laterally in conoidal fashion to create a shallow internal bevel. Cylindrical morphology in the proximal part of the wound is indicative of shear in this region, whilst the conoidal portion is suggestive of a tensile cone cracking failure mode.

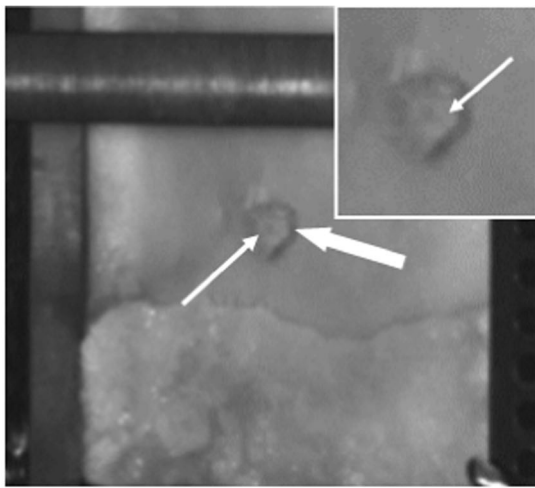
Although some deviations in trans-laminar crack path through the sandwich structures were visible, a characteristic feature of the wound cross-sections was a remarkably straight fracture edge (Fig. 6a–c). Deviations in the crack path from linearity may be attributed to inhomogeneities in bone micro-structure and in particular to the orientation of trabecular struts in relation to the advancing crack tip. Comparison of peripheral trabeculae adjacent to the trabecular fracture margin with trabeculae located further from the wound volume revealed no evidence of compressive trabecular buckling or cell collapse with permanent deformation (Fig. 6e, thick arrow). In specimens with high resolution in the trabecular region, the free edges of fractured cells along the trabecular fracture margin did not appear compressed; rather, the crack appeared to have crossed one cell width at a time through the cellular solid. When the section was parallel to the cell-axis, this process left clearly discernible bisected cells along the trabecular fracture

margin showing no signs of deformation (Fig. 6e, thin arrows). In-line fracture between angulated cortical fracture edges and trabeculae, coupled with bisection of trabeculae by a single crack, is consistent with propagation of a trans-laminar fracture through the three layers of the sandwich bone from its origin at the outer cortical surface.

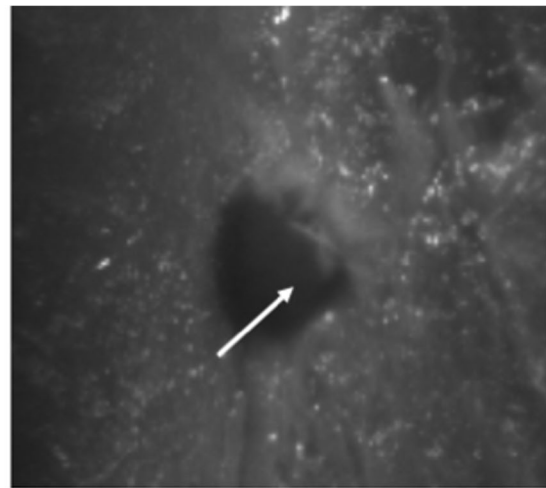
Peripheral trabeculae around the wound channel were apparently unaffected by the perforation event in all five velocity groups and regardless of absorbed energy (Fig. 6f). Trabecular attachments to the inner and outer cortical plates also remained undamaged up to the trabecular fracture margin (Fig. 6e, circled), suggesting that significant deformation of the cortical layers outside the impact location did not occur. Such structural integrity in the regions immediately around the wound channels indicates that projectile perforation from 139 to 897 m/s in sandwich bones is characterised by an extremely localised material response. One specimen in  $V_4$  and three in  $V_5$  lacked the conoidal internal structure and demonstrated a “blown out” morphology when viewed from the front, with significant fracture and elevation of the outer cortical plates. Although the exact cause of this morphology was unclear, a hydraulic bursting effect in the fluid contained within the trabecular bone is plausible. Eight wounds allowed analysis of how irregularity of the cortical entry wound related to the shape of the internal bevel. Irregular cortical entry wounds corresponded to a matching irregularity of the internal bevel in only two specimens, from groups  $V_2$  and  $V_3$ , respectively; in the other six specimens, irregular entry wounds did not result in irregular internal bevels. Analysis through the depth of the bone revealed that the fine details of cortical irregularity were lost in the trabecular fracture margin through the depth of the wound channel. This shape-deletion process is illustrated in Fig. 6g–h for a 335.55 m/s perforation event. In this specimen, the outer cortical plate displays an oval-irregular entry wound (Fig. 6g); however, the finer irregular details are lost by the trabecular fracture margin at approximately mid-depth in the trabecular lamina of the sandwich structure (Fig. 6h).

### Relationship between inner cortical plate fragments and internal fracture morphology

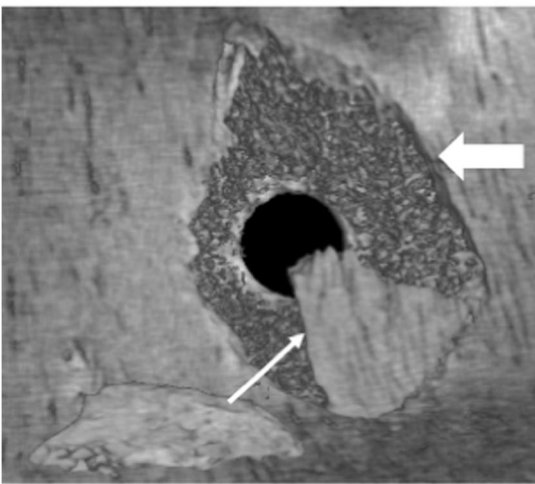
Observed relationships between the bevel and inner cortical plate fragments were consistent with trans-laminar fracture forming a distinct tri-layered conoidal structure during impact. Cross-sectional views indicated that the internal bevel was fully formed underneath retained fragment cones (Fig. 7a, arrows); this hidden bevel was found in all five  $V_1$  specimens where fragment cones obscured all or part of the exit. Sectional analysis verified that the counterpart to these inner cortical plate fragments was the exit cortical fracture edge of the internal bevel, with the two separated by the trans-laminar fracture when it reached the inner cortical plate (Fig. 7a, large



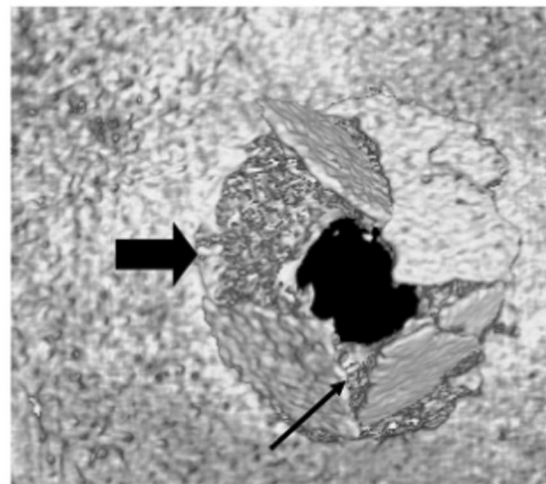
a. 142.52 m/s ( $\sigma$  0.005)



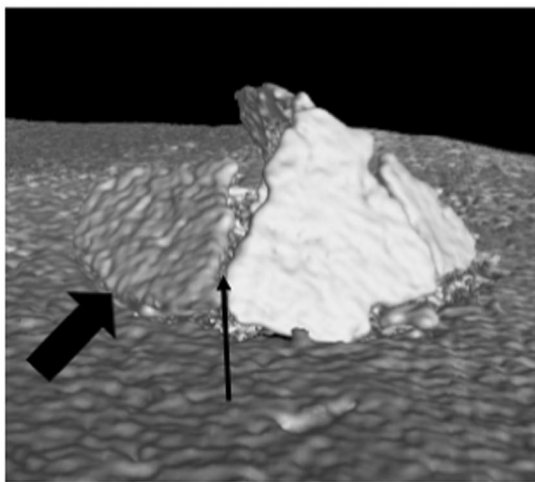
b. 333 m/s



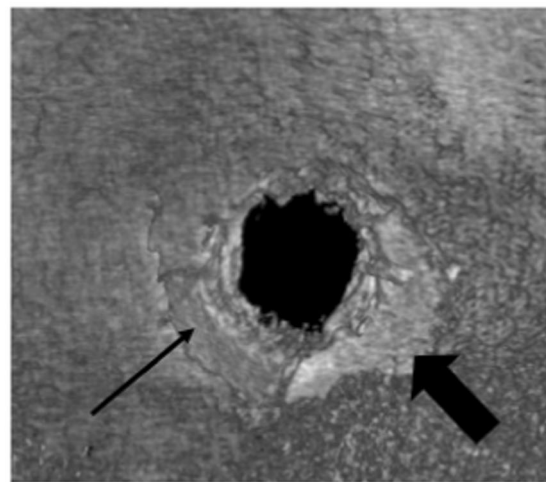
c. 166.56 m/s ( $\sigma$  0.75)



d. 167.78 m/s ( $\sigma$  0.53)



e. Fragment cone seen in d, side view



f. 718.41m/s ( $\sigma$  2.06)

arrow). Morphologically, inner cortical plate fragments with counterpart relationship to the internal bevel thus formed the floor of the conoidal wound volume. A structure

corresponding to this feature was observed in high-speed video (Fig. 4a), fully displaced from the wound and moving ahead of the projectile before its subsequent fragmentation.

**Fig. 4** High-speed footage of projectile exit and selected  $\mu$ -CT views of inner cortical plate damage; in all images, thick arrows denote the exit cortical fracture edge of the internal bevel. **a** Circular fragment of inner cortical plate dislodged from exit cortical fracture edge (thick arrow) bearing stellate fracture (thin arrow) and moving ahead of projectile, enlarged image inset highlights stellate fracture (arrow). **b** Filmed projectile exit at 333 m/s, just prior to emergence of projectile; triangular plate (arrow) indicates stellate fracture has occurred (velocity determined with time gate). **c–e** 3D images of inner cortical plate damage morphology revealed by  $\mu$ -CT of two  $V_1$  specimens; radial cracks of stellate fracture (thin arrows) arrest at the exit cortical fracture edge (thick arrows). **e** 3D side view of the fragment cone seen in **d**, with radial fracture indicated by thin arrow. **f** Rectangular, elevated cortical fragment (thin arrow) resulting from high velocity impact; note that in all images elevated fragments are circumscribed by the exit cortical fracture edge

In some sections, an accessory fracture (Fig. 7b, thin arrow) was located peripheral to the trans-laminar fracture producing the conoidal wound (Fig. 7b, thick arrow). In such cases, the presence of an angulated exit cortical fracture edge (Fig. 7b, thick arrow) indicated that the accessory fracture must have formed secondarily to the trans-laminar fracture.

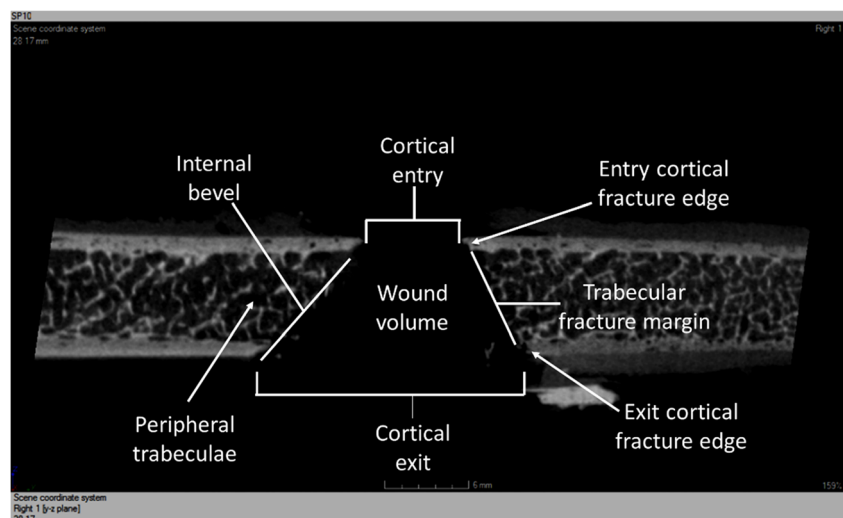
Additional evidence supporting formation of a distinct tri-layered conoidal structure was provided when the inner cortical plate fragments were in close proximity to the bevelled edge from which they were derived. Figure 7c–d shows a photograph and three-dimensional view of such a fragment on the inner cortical plate of a  $V_2$  specimen impacted at 333 m/s; the line across the fragment in Fig. 7d corresponds to the y–z view visible in Fig. 7e. In y–z section (Fig. 7e), the bevel appeared as a marked conoidal fracture in the trabecular layer with the fragment forming a partial floor to this edge of the wound. Part-counterpart relationships between exit cortical fracture edge and fragment meant the latter would slot in and out of the internal bevel in the parent bone. Observation of the whole wound from the right demonstrated the internal bevel running *underneath* the fragment (Fig. 7f), which is thus accurately interpreted as a fragment of the cortical floor of the conoidal wound. Part-counterpart association between inner

cortical plate fragments and wound were often so clear that the intact floor could be visualised even when the fragments had been significantly displaced (Fig. 7g). The conoidal fracture residing above lower cortical floor fragments and the part-counterpart relationships between them and the internal bevel was often striking (Fig. 7h). When inner cortical plate fragments showed minimal downwards displacement, the bevelled edge from which they derived was shielded from contact with a cortical shear plug or accumulated material (Fig. 7i, arrows).

## Discussion

The anatomical complexity of the human head makes detailed analyses of the terminal ballistics of this region challenging. In order to elucidate the fracture processes operative during perforation of the sandwich bone component of the head, the current study perforated pig scapulae with spherical steel projectiles and utilised a combination of  $\mu$ -CT and high-speed videography for subsequent fracture analysis. Whilst experimental conditions in the current work resulted in simpler projectile-tissue interactions than would be operative during perforation of the living bio-system, analysis of fracture morphology does not support the view that plug and spall is responsible for conoidal wound formation, as previously proposed [9–14]. Displaced inner cortical plate fragments were often in such close approximation to the bevel that a shear plug could not have been involved in bevel formation. Distinct part-counterpart relationships between inner cortical plate fragments and the internal bevel were also inconsistent with bevel formation by shear plugging. Finally, shear plug involvement in bevel formation was ruled out when the bevel was shielded behind inner cortical plate fragments. These previous features are, however, consistent with wound formation

**Fig. 5**  $\mu$ -CT image, y–z section showing cross-sectional anatomy of a perforating gunshot wound through a sandwich bone, incident velocity 335.55 m/s ( $\sigma$  1.05); see text for explanation. Projectile passed from above downwards



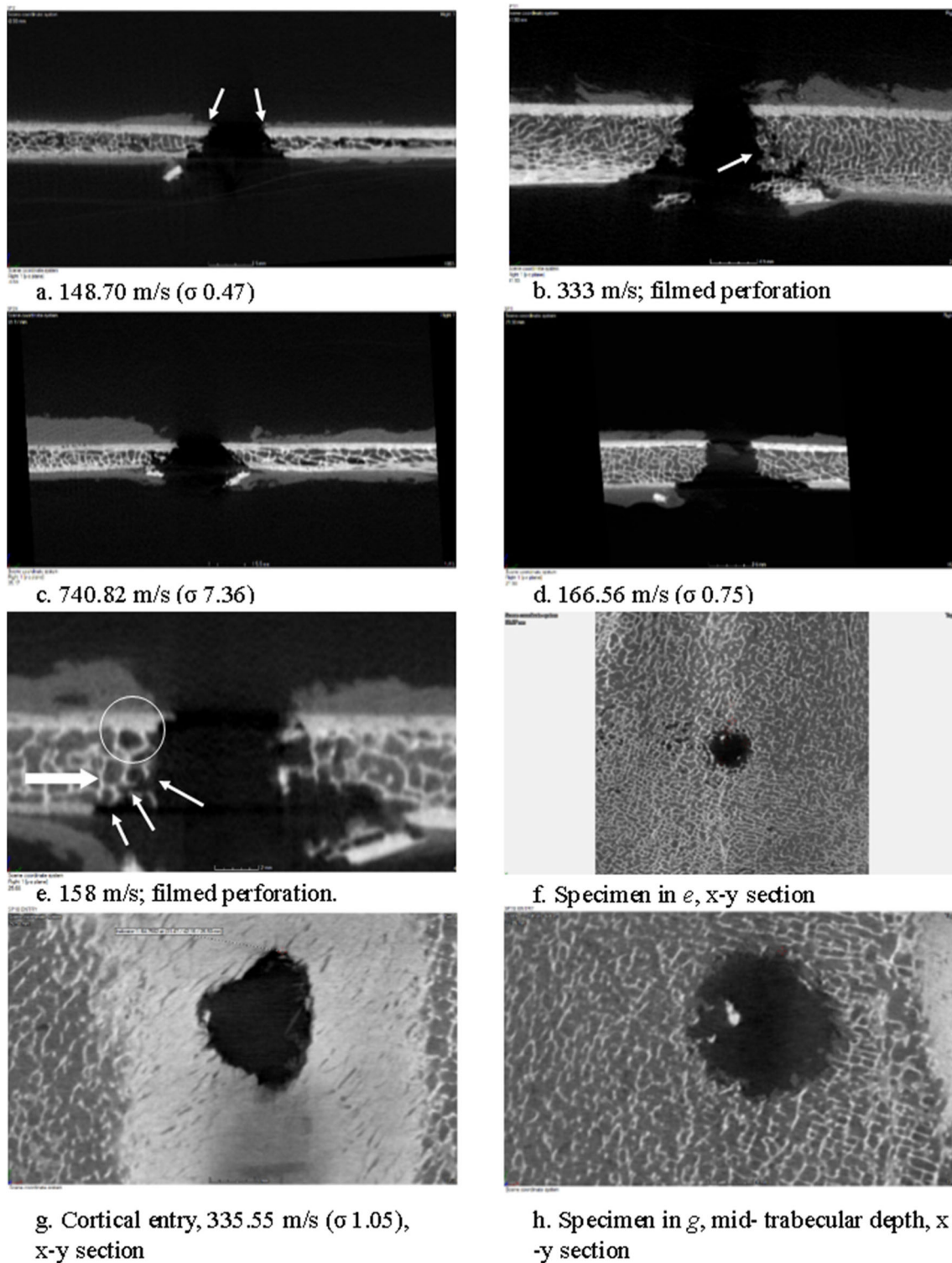


**Fig. 6**  $\mu$ -CT cross-sections of projectile wounds. **a–c** y-z views of conoidal morphology with bilateral angulation of entry cortical fracture edges (highlighted with arrows in **a**); trabecular intrusion is shown in **b** (arrow). **d** y-z section showing atypical wound cross-section. **e** Fracture morphology consistent with crack propagation one cell width at a time through trabeculae (thin arrows), y-z section. Note bilateral angulation of entry cortical fracture edges, lack of collapse of trabecular cells (thick arrow)

and intact trabecular attachments to cortex (circle). **f** x-y section of specimen seen in **e** showing localisation of wound in trabecular field. **g** x-y section of cortical entry wound in cortex. **h** x-y view of specimen shown in **g** showing loss of cortical irregularity by mid-trabecular depth. **f–h** View looking into wound from above. Incident velocities are provided with standard deviations in parentheses; velocities in **b**, **e** and **f** were determined using time gate

**Table 4** Mean entry cortical fracture edge angles for wounds exhibiting bilateral angulation of the cortices. All angles obtained from transverse (y-z) plane to eliminate any effects of bone curvature on cortical angles.

Standard deviations are in parentheses. Fracture and displacement of cortices meant accurate measurement was not possible in one\* and two\*\* specimens in groups 2, 4, and 5

Velocity group	Mean group cortical fracture edge angle, apical half	Mean group cortical fracture edge angle, basal half	Range, apical	Range, basal
1 (n = 8)	55.25 (12.19)	49.15 (7.43)	33.02–74.80	38.33–59.42
2 (n = 5)*	35.95 (3.30)	43.76 (6.48)	31.15–40.65	31.01–48.34
3 (n = 3)	54.97 (9.28)	48.99 (13.27)	41.85–61.89	39.61–58.37
4 (n = 3)**	48.13 (5.41)	42.97 (14.81)	41.35–54.60	30.65–63.79
5 (n = 5)**	47.06 (6.33)	45.51 (6.66)	36.55–53.40	39.08–54.61

by propagation of a trans-laminar fracture through the sandwich bone.

In addition to morphological features that are inconsistent with plug and spall, fundamental penetration mechanics dictates that shear plugging will not occur in all perforation events within the same material. Shear plugging is sensitive to impact angle and projectile tip shape and is commonly associated with blunt ended projectiles [22]; projectile velocity is also a contributing factor [23]. During plug formation, intense shear occurs in a cylindrical zone under and around the projectile [24]; as a result, shear plugging is associated with cylindrical plugs of approximately the same diameter as the impactor [22, 23], resulting in cylindrical perforating channels through the material. Although data for trabecular bone are lacking, cylindrical shear channels have been reported subsequent to impact in a variety of foam cores in synthetic sandwich panels [25]. Such a morphology is inconsistent with the observed morphology of conoidal wounds in sandwich bones. The contention of Symes et al. [10] that a plug of bone is pushed into the brain ahead of the projectile was not supported by the present study; projectile emergence from the inner cortical plate occurred in the absence of a sheared cortical plug in all filmed perforation events.

At present, the only other study to utilise  $\mu$ -CT to visualise the internal morphology of perforating projectile wounds to sandwich bones is that of Kieser et al. [14], who reported funnel shaped wound channels consisting of a vertical tunnel through the outer cortical layer and a conoidal bevelled region beneath this. In direct contrast, the present study found few examples where two such regions existed through the wound cross-sections. Rather than exhibiting vertical walls, the entry cortical fracture edges typically exhibited angulation suggestive of cone crack formation under the impacting projectile. Significantly, the crack induced at the cortical surface propagated through the sandwich bone without regard for the change in bone type at the upper or lower cortical-trabecular transitions. The possibility that cone cracks might form in the cortical layers of sandwich bones is supported by existing literature; cone crack formation during indentation or impact is common in brittle materials [26–28] including glass, ceramics and hard polymers [24] and has also been

demonstrated in the cortex of long bones subsequent to projectile impact [29]. A principle failure mechanism in ceramics subjected to ballistic impact is the formation of a *ceramic conoid* due to cone crack propagation; a separated conoidal volume of ceramic, flaring in the direction of projectile travel, and typically undergoing fragmentation once formed [30]. Similarity between the bevel and such conoidal fractures in other brittle materials was previously noted by Klepinger [31], although this author ultimately contended that the bevel in entry wounds was formed by shards of bone breaking free from the inner surface.

Compact bone may be classified as a bioceramic composite [32], and conoidal wounds in sandwich bones resemble observed conoidal damage in non-biogenic ceramics to a remarkable degree with the exception that there is an intervening layer of a brittle cellular solid running through the centre of the impacted structure through which the crack must propagate. However, formation of cone cracks in cellular solids is not without precedent; cone cracks have previously been reported in low density polyethylene terephthalate (PET) foams subsequent to impact [25], and morphological evidence revealed by  $\mu$ -CT suggests the involvement of cone cracks in projectile wound formation through sandwich bones. It has been established that cone cracks propagate into materials along lines of tensile stress initiating at the material surface [26] and that, when subjected to tensile stress, brittle open cell solids fail by propagation of a crack that hops one cell at a time through the material [33]. Observed trabecular fracture morphology in the present series was consistent with such a tensile failure mode; trabecular cells along the wound channel appeared to be bisected by a fracture crossing from one cell edge to another. Once initiated in the trabeculae, tensile fracture of one cell leads to greater load being borne by other cells [34]; provided enough energy is available, the fracture will thus propagate catastrophically through the entire layer [35]. Accordingly, it might reasonably be postulated that conoidal wounds are produced when a cone crack from the outer cortex propagates into and crosses the trabecular and inner cortical layers. Significantly, this process would account for the often straight-edged morphology of the trabecular fracture margin and for the lack of evidence for compression with permanent

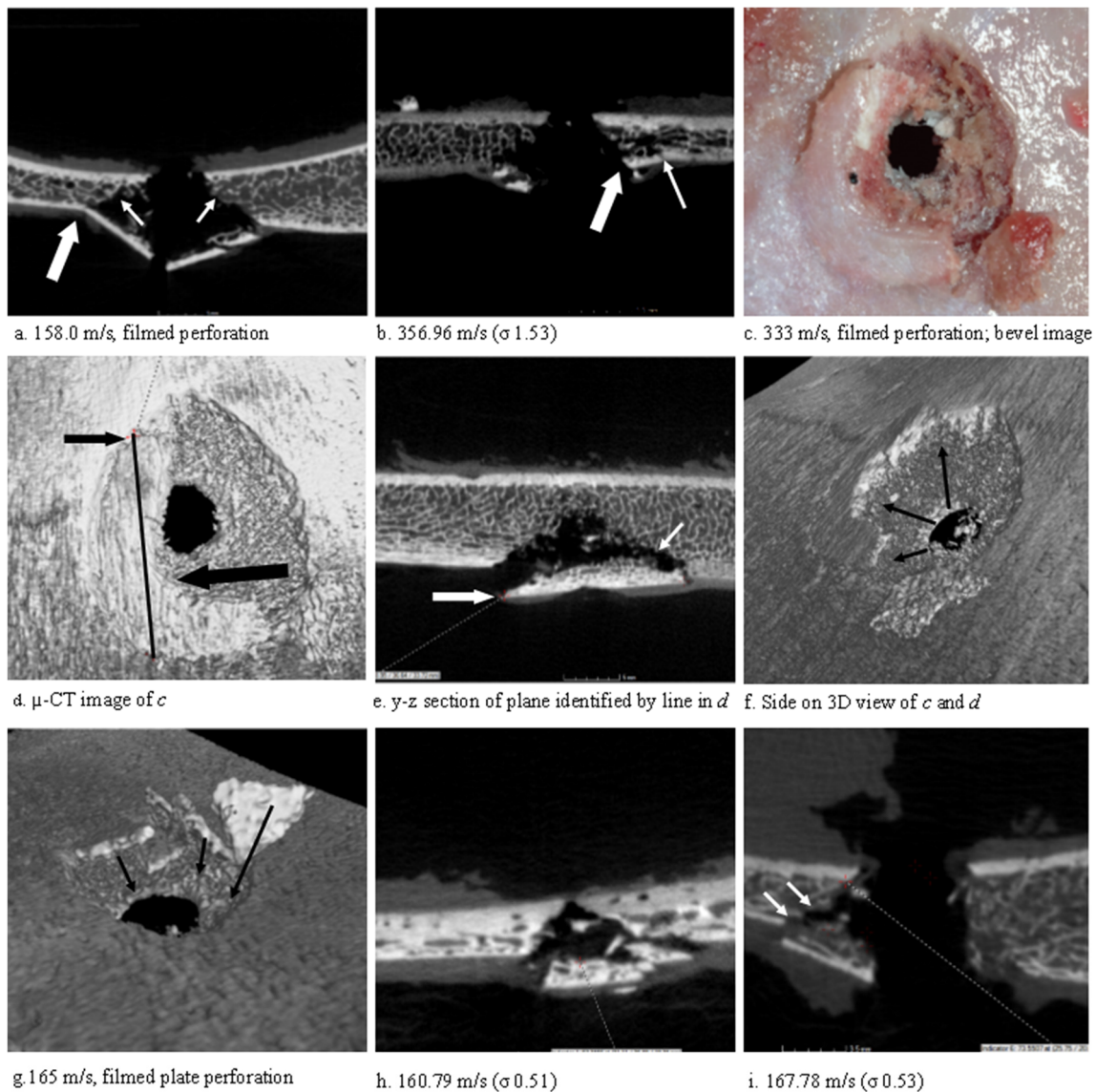


**Fig. 7**  $\mu$ -CT images of inner cortical plate damage. **a** x-z (transverse) cross-section of fragment cone with bevel concealed under fragments (arrows); large arrow marks the exit cortical fracture edge. **b** accessory cortical fracture (thin arrow) outside the exit cortical fracture edge (thick arrow), y-z section. **c** Photograph of C-shaped inner cortical plate fragment partially covering internal bevel after a 333-m/s perforation. **d**  $\mu$ -CT 3D view of fragment shown in **c**; black line shows plane of slice visible in **e**. **e** y-z view of C-shaped fragment, viewed in direction of large arrow shown in **d**; note the conoidal internal bevel above the fragment and the close approximation between bevel

and fragment at right of image, with just over 1 mm separation in the region identified by the small arrow. Left hand arrows in **d** and **e** point to the elevated side of the fragment. **f** 3D view looking under C-shaped fragment in **c–e**; viewed from the right side, the internal bevel can be seen running underneath the fragment (arrows). **g** 3D view looking into a conoidal wound from  $V_1$ ; fragments moved in direction of arrows would partially re-form the floor of the wound. **h** Marked conoidal fracture and counterpart fragments, y-z section. **i** x-z section of bevelled edge (arrows) protected behind inner cortical plate fragment

deformation of trabecular cells lining the wound channel, a feature also noted by Kieser et al. [14].

An issue of central importance to the cone crack hypothesis is the question of how such a fracture crosses the upper and lower interfaces between cortices and trabeculae. Whether a given fracture will arrest, be deflected by or cross a given interface between two materials is determined by the angle of the fracture relative to the interface, the difference in elastic moduli between the two materials and the presence of a third interface material sandwiched between the other two [36, 37].

When considering crack propagation from cortical to trabecular bone, the latter component may be eliminated due to lack of interface material between bone types. The relationship between fracture angle and the probability of a fracture crossing or deflecting an interface is analogous to the process of skimming a stone over water; the more acute the angle, the greater the probability that the fracture will be deflected along the interface, rather than penetrating it [38]. In the present analysis, no crack deflection was observed at the interfaces between cortical and trabecular bone, suggesting that cortical

fracture angles are above the critical limit for crack deflection at the interfaces.

The relative elastic moduli of the two materials is of particular importance to crack behaviour at an interface; when a fracture approaches an interface with a material of lower elastic modulus, crack velocity increases significantly [39] and the crack is thus more likely to propagate into the second material. Although there is a wide range of reported values for the elastic modulus of trabecular bone in the literature, Keaveny et al. [40] summarised data for elastic moduli determined using ultrasound methods and found values approximately 20% lower than that for cortical bone. More recent analyses have suggested that the elastic modulus of trabecular bone is lower than that of cortical bone, but only slightly [40, 41]. In sandwich bones, direct continuity between cortices and trabeculae and abundant cortical-trabecular connections, coupled with elastic modulus mismatch, would enhance the probability of a given fracture propagating into the trabecular layer from the outer cortex. Based upon internal and external fracture morphology and the above theoretical considerations, a novel mechanism for conoidal wound formation through sandwich bones is described below and in diagrammatic form in Fig. 8:

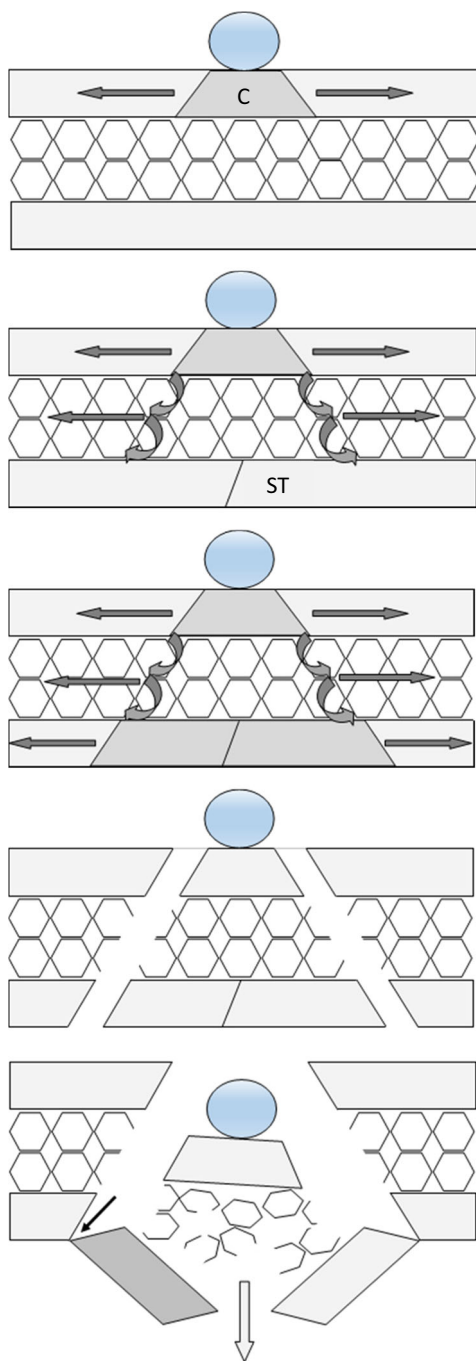
1. Projectile impact initiates the formation of a cone crack within the outer cortical plate.
2. The cortical cone crack propagates across the upper cortical-trabecular transition via trabecular attachments that are in line with the cortical tensile stress. Tensile failure causes propagation of the crack across the trabecular cells one cell width at a time and produces a relatively straight-edged trabecular fracture margin. Local inhomogeneities in trabecular composition and differences in trabecular orientation may cause the crack to deviate and result in trabecular intrusion into the wound channel. High tensile stresses begin formation of stellate fractures on the inner cortical plate before projectile exit.
3. The cone crack propagates from the lower trabeculae through to the inner cortical layer via trabecular attachments in line with the tensile stress trajectory.
4. Propagation of the fracture to the lower cortical table completes formation of the internal bevel and results in formation of a conoidal volume of bone consisting of all three layers of the sandwich bone separated from the parent bone by the bevel. This structure remains intact during low-velocity impacts.
5. Kinetic energy and stress waves associated with high-velocity impacts result in the instantaneous collapse and fragmentation of the formed conoidal volume. The floor of this volume forms *inner cortical plate fragments* which undergo elevation and eversion during projectile exit, leaving fragment cones at low velocity. At higher velocity, these fragments are largely ejected with soft tissue

components, although some may remain in situ due to incomplete trans-laminar fracture or retention within soft tissue. Trans-laminar fracture results in part-counterpart relationships between these retained fragments and the internal bevel.

According to this mechanism, the internal bevel is the counterpart to the missing bone volume which, if intact, would slot in and out of the parent bone. The intact conoidal bone volume produced by this mechanism would be identical to the ceramic conoids produced in engineering ceramics subjected to ballistic impact, where a conoid of material is separated from the parent ceramic by the conoidal fracture [30]. In the bone, such a conoidal volume may thus reasonably be termed a *bioceramic conoid*. Once initiated, cone cracks will propagate at the speed of sound for the material in which they are propagating, with conoid formation typically only taking a few microseconds in engineering ceramics [42]. Whilst the plug and spall hypothesis proposes that the bevel is created during projectile exit [9–12], the cone crack hypothesis suggests it is created *at the moment of impact*; the bevel is then revealed by subsequent conoid fragmentation. Additional evidence that bevel formation is due to trans-laminar fracture arises from the observation that bevels are interrupted at pre-existing fractures or sutures; this process, known as crack arrest, occurs when the energy driving fracture dissipates at the discontinuity [43].

Although the cone crack hypothesis suggests that wound formation is driven by tensile stress, this does not preclude the simultaneous operating of other failure modes through the wound volume; indeed, most cracks in bone are formed under a mixture of stresses [44]. Observation of stellate fracture patterns in the inner cortical plate confirms that a compressive stress transfers through the conoid during perforation, resulting in eventual tensile failure there. High-velocity perforation also undoubtedly involves additional mechanisms such as stress wave induced trabecular cell collapse [45], delamination within cortical bone [19] and possibly heating effects [14]. Previous scanning electron microscope analysis of entry cortical fracture edges in bovine (*Bos taurus*) sandwich bones has identified fracture surfaces produced by tensile failure [19]. However, further fracture surface characterisation in both human and non-human bone is required to test the hypothesis that wound formation is driven by tensile stress and also to establish the contribution of additional failure modes to projectile wounding.

In the present experiment, no intact bioceramic conoids were produced and fracture through the sandwich bones was often incomplete, with portions of the conoid floor remaining attached to the exit cortical fracture edge. The rarity of intact bioceramic conoids reported in case work suggests a particular set of circumstances must combine to form them; kinetic



Step 1. Projectile impact initiates formation of a cone crack (C) under tension (arrows) in the outer cortical plate.

Step 2. The cone crack enters the trabecular layer via trabeculae orientated along the lines of tensile stress; under tension, the crack jumps from one cell strut to another (curved arrows). Compressive stress passing through the sandwich bone results in tensile failure of the inner cortical plate and formation of a stellate fracture radiating from the centre (angulated line ST).

Step 3. The cone crack follows lines of tensile stress into the inner cortical plate.

Step 4. Crack propagation through the entire sandwich structure results in temporary formation of a bioceramic conoid, separated from the parent bone by the internal bevel.

Step 5. During higher velocity impacts, trabeculae undergo stress-wave induced cell collapse. As the conoidal volume compresses, full failure of the inner cortical plate occurs in the centre at the stellate fracture (open arrow). After impact, some of the cortical floor may remain as *inner cortical plate fragments* (dark grey section of inner plate). Trans-laminar fracture results in part-counterpart relationships between these retained fragments and the internal bevel (solid arrow).

**Fig. 8** Novel mechanism for conoidal wound formation through sandwich bones

energy absorption must be low enough to prevent fragmentation and trans-laminar fracture must entirely separate the conoid from the parent bone. In brittle materials, plug fragmentation is likely to occur at velocities 5–10% above the minimum perforation velocity [22]; with higher velocity impacts, it is therefore to be expected that much of the bioceramic conoid would undergo fragmentation. Such behaviour is also consistent with engineering ceramics, where fragmentation is similarly restricted to the separated conoid [24]. Impact data generated in the present study revealed that incident velocity and

energy absorption were positively correlated. The law of conservation of energy dictates that both greater fragmentation and greater energy utilisation in fragment ejection must occur as velocity increases, with the latter process becoming particularly significant at higher velocities [46]. A positive correlation between incident velocity and energy absorption has also been found in synthetic sandwich panels, where it is thought to be a characteristic of such structures [47, 48].

It is generally held that perpendicular entry wounds tend to be circular or oval in shape [5] and also that areas of bevel



elongation indicate projectile trajectory [6, 7]. The current study substantiated the high frequency of circular wounds, which accounted for just under half of all cortical entry shapes. Whilst oval and irregular wounds were more common at higher velocities, circular wounds were present in the lowest and highest velocity groups. Variation in cortical entry wound shape subsequent to perpendicular impact with spherical, non-deforming projectiles suggests the importance of intrinsic biological factors, such as bone microarchitecture, in determining wound shape. The frequency of bevel asymmetry was interesting; of 14 circular wounds, 12 (85.71%) exhibited asymmetrical bevelling. Across all cortical entry shapes, asymmetrical bevelling was far more common than symmetrical bevelling, accounting for 82.76% of bevels. These findings are in accordance with previously published data for entry wounds in human crania [21], where only 15% of bevels were classed as symmetrical; an exact correlation between trajectory and bevel asymmetry was found in only five out of 39 entry wounds. In light of these findings, these authors highlighted the importance of intrinsic anatomical features in determination of bevel shape.

Observation of projectile exit in the present analysis suggested that the bevel and its symmetry are determined before projectile exit has occurred, with accessory fractures outside the conoidal wound potentially contributing to apparent bevel asymmetry. The cone crack hypotheses predicts that bevel shape would be determined by the initial angle of the cone crack, which differs around the cortical entry wound, and the subsequent crack path through the trabecular network. In synthetic materials, cone cracks become steeper with a decrease in Poisson's ratio [49] and with an increase in velocity [26]. Although further work is required to investigate relationships between velocity and cone angle in bone, overlap between angles across the velocity groups suggests that material factors might supersede loading rate in determining the angles achieved. Upon establishment of the cone angles in the outer cortex, final bevel shape would be determined by the subsequent path of the cone crack through the trabecular layer and inner cortex. High frequency of bevel asymmetry with perpendicular impacts suggests caution should be applied when using this feature to make trajectory determinations in the absence of an exit wound or other directionality indicators.

A number of authors have noted that irregular cortical entry wounds do not always result in irregular internal bevels [13, 21]. These findings were supported by the present study; irregular or partially irregular entry shape was lost by the internal bevel in 80% of irregular wounds.  $\mu$ -CT analysis revealed that fine details of cortical irregularity are deleted by approximately mid-depth in the trabecular layer. This phenomenon is consistent with the hypothesis of wound formation by trans-laminar cone crack propagation; minor deviations in crack path through individual trabeculae and differences in

trabecular orientation in relation to the advancing crack would have a distorting effect as it propagated downwards, resulting in a deletion of information relating to entry wound shape as depth increased.

Despite lack of production of intact bioceramic conoids, comparison of plug morphology produced by low-velocity impacts [15–17] with residual fracture morphology subsequent to medium and high-velocity impacts reveals similarities that are indicative of a common fracture process. Whilst overlap in external morphology between conoidal wounds produced by blunt and projectile trauma has been reported previously [50–52], this is the first report of wounds inflicted at 150 m/s being identical internally to those produced at 850 m/s. These shared internal and external morphological features suggest that conoidal wounds form a distinct category of trauma characterised by trans-laminar crack propagation and bioceramic conoid production. In cross-section, such conoidal wounds may be diagnosed by angulated entry cortical fracture edges in all or parts of the section and by evidence for crack propagation through all three layers of the sandwich bone. Further work utilising low-velocity impacts is required to confirm their wider role in wound formation. The hypothesis that trans-laminar fracture underlies formation of all conoidal wounds raises interesting research challenges for enhanced differential diagnosis.

In addition to overlap between trauma types, wound diagnosis is complicated by taphonomic agencies including rodent gnawing [53] and carnivore scavenging [54]. Diagnosis may also be complicated by deliberate anthropogenic activities, particularly the use of fire [55, 56]. Traumatic wounds must also be differentiated from pseudotraumatic defects [57] such as missing sutural ossicles, which can combine with other fractures to create defects resembling those produced by traumatic events [58]. Cross-sectional microanatomy revealed by  $\mu$ -CT provided a number of features that might be of diagnostic value. Sandwich bone response to projectile perforation was found to be extremely localised. Damage localisation is due to the short contact time between impactor and target, resulting in kinetic energy absorption over a small area [59]. Localisation of damage is also a characteristic feature of impacted cellular solids [45], and internal examination of perforated sandwich bones revealed intact peripheral trabeculae even at the highest velocities. Conoidal wounds exhibited angulation of the entry cortical fracture edges, trans-laminar fracture through the trabeculae which crossed from one cell edge to another, lack of sandwich layer delamination and lack of permanent collapse of trabecular cells. Further work with lower velocity impact events is needed to detect when such features appear; comparative work with pseudotraumatic defects is also essential. Elucidation of the taphonomic resistance of any identified diagnostic indicators is also critical if they are to be of use in skeletal remains subjected to deposition in ecosystems.

**Acknowledgements** We are indebted to Dr. David Wood, Andrew Taylor, David Miller and Alan Peare for their considerable technical input and for operation of the gas guns and projectile housing. We would also like to extend our thanks to Kerrie Smith for the error propagation formula and Dr. Keith Rogers and George Adams for their assistance and advice with micro-computerised tomography.

## Compliance with ethical standards

**Conflict of interest** The authors declare that they have no conflict of interest.

**Ethical approval** This study was approved by the ethics committee of Cranfield University.

## References

- Maiden N (2009) Ballistics reviews: mechanisms of bullet wound trauma. *Forensic Sci Med Pathol* 5:204–209. <https://doi.org/10.1007/s12024-009-9096-6>
- Aarabi B, Tofighi B, Kufera JA, Hadley J, Ahn ES, Cooper C, Malik JM, Naff NJ, Chang L, Radley M, Kheder A, Uscinski RH (2014) Predictors of outcome in civilian gunshot wounds to the head. *J Neurosurg* 120:1138–1146
- Mota A, Klug WS, Ortiz M, Pandolfi A (2003) Finite-element simulation of firearm injury to the human cranium. *Comput Mech* 31:115–121. <https://doi.org/10.1007/s00466-002-0398-8>
- Snell RS (1995) *Clinical anatomy*. Lipincott Williams and Wilkins, Maryland
- Berryman HE, Symes SA (1998) Recognising gunshot and cranial trauma through fracture interpretation. In: Reichs KJ (ed) *Forensic osteology: advances in the identification of human remains*. Charles C Thomas Publishers, Springfield, pp 333–352
- Rhine and Curran (1990) Multiple gunshot wounds to the head: an anthropological review. *J Forensic Sci* 35(3):1236–1245
- Spitz WU (2006) Injuries by gunfire. In: Spitz WU, Spitz DJ, Clark R (eds) *Spitz and Fisher's medicolegal investigation of death: guidelines for the application of pathology to crime investigation*. Charles C Thomas Publishers, Springfield Available from: Proquest Ebook Central. Accessed 9.11.17
- Hull D (1999) *Fractography: observing, measuring and interpreting fracture surface topography*. Cambridge University Press, Cambridge
- Komar DA, Buikstra JE (2008) *Forensic anthropology: contemporary theory and practice*. Oxford University Press Inc., New York
- Symes SA, L'Abbé EN, Chapman EN, Wolff I, Dirkmaat DC (2012) Interpreting traumatic injuries to bone in medicolegal investigations. In: Dirkmaat DC (ed) *A companion to forensic anthropology*. Wiley-Blackwell Publishing, West Sussex
- Christensen AM, Passalacqua NV, Bartelink EJ (2014) *Forensic anthropology: current methods and practice*. Academic Press, Oxford
- Peterson BL (1991) External beveling of cranial gunshot entrance wounds. *J Forensic Sci* 36(5):1592–1595
- Kimmerle EH, Baraybar JP (2008) *Skeletal trauma: identification of injuries resulting from human rights abuses and armed conflict*. CRC Press, Florida
- Kieser JA, Tahere J, Agnew C et al (2011) Morphoscopic analysis of experimentally produced bony wounds from low velocity ballistic impact. *Forensic Sci Med Pathol* 7:322–332. <https://doi.org/10.1007/s12024-011-9240-y>
- Murphy MS, Gaither C, Goycochea E, Verano JW, Cock G (2010) Violence and weapon-related trauma at Puruchuko-Huaquerones, Peru. *Am J Phys Anthropol* 142:636–649
- Murphy MS, Spatola B, Weathermon R (2014) Allies today, enemies tomorrow: a comparative analysis of perimortem injuries along the biomechanical continuum. In: Martin DL, Anderson CP (eds) *Bioarchaeological and forensic perspectives on violence: how violent death is interpreted from skeletal remains*. Cambridge University Press, Cambridge, pp 261–288
- Bird CE, Fleischman JM (2015) A rare case of an intact bone plug associated with a gunshot exit wound. *J Forensic Sci* 60(4):1074–1077
- Smith MJ, Brickley MB, Leach SL (2007) Experimental evidence for lithic projectile injuries: improving identification of an under-recognised phenomenon. *J Archaeol Sci* 34:540–553
- Rickman JM, Smith MJ (2014) Scanning electron microscope analysis of gunshot defects to bone: an underutilised source of information on ballistic trauma. *J Forensic Sci* 59(6):1473–1486. <https://doi.org/10.1111/1556-4029.12522>
- Currey JD (2002) *Bones: structure and mechanics*. Princeton University Press, New Jersey
- Quatrehomme G, İşcan MY (1998) Analysis of bevelling in gunshot entrance wounds. *Forensic Sci Int* 93:45–60
- Zukas JA (1982) Penetration and perforation of solids. In: Zukas JA, Nicholas T, Swift HF, Greszczuk LB, Curran DR (eds) *Impact dynamics*. John Wiley and Sons, Inc., USA, pp 155–214
- Backman ME, Goldsmith W (1978) The mechanics of penetration of projectiles into targets. *Int J Eng Sci* 16:1–99
- Crouch IG (2016) An introduction to armour materials. In Crouch IG, Arthur J (eds) *The science of armour materials*, available from ProQuest Ebook central
- Hassan MZ, Cantwell WJ (2012) The influence of core properties on the perforation resistance of sandwich structures: an experimental study. *Compos Part B* 43:3231–3238
- Knight CG, Swain MV, Chaudhri (1977) Impact of small steel spheres on glass surfaces. *J Mater Sci* 12:1573–1586
- Chen SY, Farris TN, Chandrasekar S (1995) Contact mechanics of Hertzian cone cracking. *Int J Solids Struct* 2(3/4):329–340
- Lawn BR (1998) Indentation of ceramics with spheres: a century after Hertz. *J Am Ceram Soc* 81(8):1977–1994
- Kieser DC, Riddell R, Kieser JA, Theis J, Swain MV (2013) Bone micro-fracture observations from direct impact of slow velocity projectiles. *J Arch Mil Med* 2(1):e15614. <https://doi.org/10.5812/jamm.15614>
- Zaera R, Sánchez-Gálvez V (1998) Analytical modelling of normal and oblique ballistic impact on ceramic/metal lightweight armours. *Int J Impact Eng* 21(3):133–148
- Klepinger LL (2006) *Fundamentals of forensic anthropology*. John Wiley & Sons, New Jersey
- Olszta MJ, Cheng X, Jee SS, Kumar R, Kim YY, Kaufman MJ, Douglas EP, Gower LB (2007) Bone structure and formation: a new perspective. *Mater Sci Eng R Rep* 58:77–116
- Gibson LJ, Ashby MF (1988) *Cellular solids: structure and properties*. Pergamon press, Oxford
- Kaplan SL, Hayes WC, Stone JL (1985) Tensile strength of bovine trabecular bone. *J Biomech* 18(9):723–727
- Tomar V (2009) Insights into the effects of tensile and compressive loadings on microstructure dependent fracture of trabecular bone. *Eng Fract Mech* 76:884–897
- Imbeni V, Kruzic JJ, Marshall GW, Marshall SJ, Ritchie RO (2005) The dentin-enamel junction and the fracture of human teeth. *Nat Mater*. <https://doi.org/10.1038/nmat1323>
- Zimmermann EA, Gludovatz B, Schaible E, Busse B, Ritchie RO (2014) Fracture resistance of human cortical bone across multiple length scales at physiological strain rates. *Biomaterials* 35:5472–5481

38. He M-Y, Hutchinson JW (1989) Crack deflection at an interface between dissimilar elastic materials. *Int J Solids Struct* 25(9):1053–1067
39. Mencik J (2010) *Mechanics of components with treated or coated surfaces*. Klewer Academic Publishers, Netherlands
40. Keaveny TM, Morgan EF, Yeh OC (2004) Bone biomechanics. In: Kutz M (ed) *Standard handbook of biomedical engineering and design*. McGraw-Hill Professional, USA, pp 8.1–8.23
41. Bayraktar HH, Morgan EF, Niebur GL, Morris GE, Wong EK, Keaveny TM (2004) Comparison of elastic and yield properties of human femoral trabecular and cortical bone tissue. *J Biomech* 37:27–35
42. Kaufmann C, Cronin D, Worswick M, Pageau G, Beth A (2003) Influence of material properties on the ballistic performance of ceramics for personal body armour. *Shock Vib* 10:51–58
43. Madea B, Staak M (1988) Determination of the sequence of gunshot wounds of the skull. *J Forensic Sci Soc* 28:321–328
44. Zimmermann EA, Launey ME, Barth HD, Ritchie RO (2009) Mixed mode fracture of human cortical bone. *Biomaterials* 30: 5877–5884
45. Zou Z, Reid SR, Tan PJ, Li S, Harrigan JJ (2009) Dynamic crushing of honeycombs and features of shock fronts. *Int J Impact Eng* 36: 165–176
46. Abrate S (1998) *Impact on composite structures*. Cambridge University Press, Cambridge
47. Skvortsov V, Kepler J, Bozhevolnaya E (2003) Energy partition for ballistic penetration of sandwich panels. *Int J Impact Eng* 28:697–716
48. Hou W, Zhu F, LU G, Fang D-N (2010) Ballistic impact experiments of metallic sandwich panels with aluminium foam core. *Int J Impact Eng* 37:1045–1055
49. Chaudhri MM (2015) Dynamic fracture of inorganic glasses by hard spherical and conical projectiles. *Philos Trans R Soc Lond A* 373:20140135. <https://doi.org/10.1098/rsta.2014.0135>
50. Spatola BF (2015) Atypical gunshot and blunt force injuries: wounds along the biomechanical continuum. In: Passalacqua NV, Rainwater CW (eds) *Skeletal trauma analysis: case studies in context*. John Wiley & Sons, West Sussex, pp 7–26
51. Quatrehomme G, Piercecchi-Marti M, Buchet L, Alunni V (2015) Bone bevelling caused by blunt trauma: a case report. *Int J Legal Med* 130(3):771–775. <https://doi.org/10.1007/s00414-015-1293-0>
52. Vermeij EJ, Zoon PD, Chang SBCG, Keereweer I, Pieterman R, Gerretsen RRR (2012) Analysis of microtraces in invasive traumas using SEM/EDS. *Forensic Sci Int* 214(1):96–104
53. Nawrocki SP (2009) Forensic taphonomy. In: Blau S, Ubelaker DH (eds) *Handbook of forensic anthropology and archaeology*. Left Coast Press, California, pp 284–294
54. Moraitis K, Spiliopoulou C (2010) Forensic implications of carnivore scavenging on human remains recovered from outdoor locations in Greece. *J Forensic Legal Med* 17:298–303
55. Pope EJ, Smith O'BC (2004) Identification of traumatic injury in burned cranial bone: an experimental approach. *J Forensic Sci* 49(3):1–10
56. Tümer AR, Karacaoğlu E, Keten A, Ünal M (2012) Postmortem burning of the corpses following homicide. *J Forensic Legal Med* 19:223–228
57. Loe L (2009) Perimortem trauma. In: Blau S, Ubelaker DH (eds) *Handbook of forensic anthropology and archaeology*. Left Coast Press, California, pp 263–283
58. Machado MPS, Simões MP, Gamba TO, Flores IL et al (2016) A Wormian bone, mimicking a gunshot entrance wound of the skull, in an anthropological specimen. *J Forensic Sci* 61(3):855–857. <https://doi.org/10.1111/1556-4029.13043>
59. Cantwell WJ, Morton J (1989) Comparison of low and high velocity impact response of CFRP. *Composites* 20(6):545–551